Check for updates

Extending quantum coherence lifetimes in nonadiabatic dissipative molecular systems with chirped pulses†

Robert Strich, [ID] Shirin Faraji [ID] and Elisa Palacino-González [ID] *

Quantum coherences play a central role in a broad range of fields, including functional energy materials, biological systems, and molecular quantum information science. Coherences encode critical information about the phase and dynamics of a system, and their interaction with its environment. Particularly, the ultrafast charge transfer process between electron donor and acceptor species in functional energy materials is influenced by vibronic coherences. A key limitation arises from the dephasing of coherences due to dissipation, causing loss of information and limiting applications of molecular systems. Extending and controlling coherence lifetimes would enable the rational design of smarter materials with optimised properties. Here we introduce a novel idea using chirped excitations as a pathway to extend quantum coherence lifetimes, enhancing their robustness against dissipation. A detailed analysis of the light-induced molecular quantum dynamics and wave packet evolution from first-principles models constructed at the donor–acceptor heterojunction of an organic photovoltaic blend is discussed. We demonstrate that tuning the chirp of the excitation pulse, vibronic coherence lifetimes can be extended up to the picosecond timescale. Chirped excitations also enable tunable spatial localisation of the induced wave packet, with localisation controlled by the chirp intensity. These effects are observed consistently across different donor–acceptor adducts selected from the molecular dynamics structure of the blend. Our results introduce a new degree of freedom for coherent control in molecular systems, offering a promising pathway toward the development of advanced functional energy materials and applications in molecular quantum information science.

1 Introduction

Quantum (electronic, vibrational and vibronic) coherences in molecular systems play a crucial role in many ultrafast physical, chemical, and biological processes.[4,6,45,49] The preservation of phase relationships between quantum states, a property inherent to coherences, is key to mechanisms such as ultrafast charge and energy transfer in functional molecular materials,[28,48] efficient light harvesting in photosynthetic complexes,[39] and the development of quantum information technologies using molecular platforms.[47,60] This associated phase to any superposition state in quantum mechanics can be viewed as information between the excitation and the two states resonant to it. Hence having the possibility to manipulate these coherences could unlock new possibilities for advancing molecular-scale electronics, engineering precise light–matter interactions or enhancing energy transport. A persistent challenge in exploiting quantum coherences lies precisely on a property inherent to coherences, namely, dephasing. In molecular physics, the interaction with a dissipative environment, such as solvent fluctuations or phonon coupling, lead to rapid dephasing, thereby destroying the phase information previously encoded in the system.

Achieving precise control over quantum processes in molecules remains a central barrier. Molecular systems feature fast, coupled electronic and nuclear motion that is highly sensitive to the environment. Designing laser pulses that can steer such dynamics with fidelity is non-trivial, especially when decoherence and dissipation play a role. Additionally, translating theoretical control schemes into experimentally feasible protocols often faces limitations in pulse shaping and system characterization. As a result, considerable effort has been devoted to developing approaches for coherent control of molecular systems with external pulses.[5,7,8,11,22,25,29,42,44,51,59,62–64,66,67] In this context, ultrafast shaped laser pulses are tailored in amplitude, phase, or polarization to drive specific quantum pathways. Pulse shaping has proven to be a versatile tool for tailoring excitation conditions to extend coherence lifetimes and steer molecular

Institute of Theoretical and Computational Chemistry, Heinrich-Heine Universität Düsseldorf, Germany. E-mail: elisa.palacino.gonzalez@hhu.de

† Authors dedicate this paper to Prof. Christel Marian on the occasion of her 70th birthday.

dynamics with high precision. Early experimental[27] and theoretical studies[37] on control with tailored femtosecond pulses laid the groundwork for this field, revealing the potential of shaped femtosecond pulses to selectively control vibrational excitation and molecular dissociation pathways. Later theoretical studies[14,50] have significantly advanced the theoretical framework of this field, demonstrating how shaped pulses can be used to manipulate nonadiabatic transitions, entangle electronic and vibrational degrees of freedom, and explore the coherent control of photo-induced processes in molecular systems. Their work emphasizes the sensitivity of vibronic coherence evolution to both the spectral content and phase structure of excitation pulses, underscoring the need for fine pulse design in coherent control protocols. Among pulse shaping techniques, linearly chirped pulses have attracted particular interest over the past decades. Several theoretical and experimental studies have shown that chirped excitations provide an additional degree of freedom to control the temporal ordering of excitation pathways and the population of vibronic states.[2,3,9,13,24,31–34,38,53,55] For example, they can effectively enhance coherence excitations and be used to manipulate vibronic populations and coherence dynamics in molecular systems, revealing their potential to uncover rich dynamical information from complex molecular systems.

Building on prior work by some of the present authors,[53] on a minimal model with charge-transfer signatures to investigate the effect of chirped excitation on double-pump femtosecond fluorescence spectroscopic signals, here an advancement is presented. This prior work revealed that chirped pulses can reduce long-term charge-transfer population and enable selective tuning of short-time dynamics *via* modulation of wavepacket motion. Built on this, double-pump fluorescence signals revealed that chirped excitation enhanced vibrational signatures in fluorescence spectra, offering better interpretability under low-signal-to-noise ratio. Tested on a physical model, these findings lay the foundation for the work introduced here, where the model is improved to include a first-principles description of a charge-transfer dimer from a prototypical organic photovoltaic blend. Besides, a detailed analysis of quantum coherences lifetime, in the presence of dissipation, is described alongside its connection with the properties of the chirped excitation. A first-principles Hamiltonian is constructed using time-dependent density functional theory (TDDFT) calculations in combination with molecular dynamics (MD) simulations for describing the intermolecular charge-transfer process in a prototypical organic photovoltaic blend. A detailed analysis of the role of chirped excitations for manipulating the system quantum dynamics is presented. Particularly, we demonstrate that the lifetime of quantum coherences can be significantly extended by using chirped excitations. Our results indicate that chirped excitation induces a vibronic wave packet with a substantially longer coherence lifetime compared to that generated by a transform-limited (TL) pulse. Importantly, this extension is tunable, with longer lifetimes observed at higher chirp rates. In addition, chirped pulses lead to greater localization of the wave packet, enhancing the vibronic character of the system. These insights not only advance our understanding of quantum coherence evolution under shaped laser fields but also suggest promising strategies for designing coherence-preserving quantum control protocols in dissipative environments, with potential applications in quantum information science[45,47,60] and advanced functional energy materials.[18]

The remainder of this paper is organized as follows. Section 2 outlines the theoretical methodology employed throughout this work. We begin by presenting the formalism used to describe the system and its interaction with a dissipative environment, focusing on ultrafast intermolecular charge transfer in a prototypical organic photovoltaic (OPV) blend, the poly(3-hexylthiophene):phenyl-C61-butyric acid methyl ester (P3HT:PCBM).[1,12,17,20,21,23,26,36,43,52,56,58,65] We detail the first-principles approach developed to model the dimer adduct at the heterojunction, followed by a discussion of the dissipative environment arising from the blend. Subsequently, we introduce the concept of linearly chirped pulses and describe the system–field Hamiltonian utilized in our simulations. The section concludes with a presentation of the quantum master equation governing the time evolution of the system in the presence of the dissipative environment. Section 3 presents the results, including an analysis of the population dynamics and wave packet evolution (Section 3.1), Wigner function representations and quantum coherences (Section 3.2), and additional results for an alternative model system based on a different dimer configuration within the blend (Section 3.3). Finally, Section 4 provides concluding remarks and perspectives for future work. The SI is provided in a separate file and contains a detailed account of the numerical methods employed, including TDDFT and MD simulations, molecular orbital analyses, and additional data from the quantum dynamical simulations.

2 Theoretical methodology

2.1 Reduced density matrix formalism and overall Hamiltonian

To investigate the influence of femtosecond optical chirped pulses on the charge-transfer process within the dissipative environment of the organic photovoltaic blend, we adopt a reduce density matrix formalism where the overall Hamiltonian is given by

$$H = H_S + H_B + H_{SB}. \tag{1}$$

Here, H_S denotes the Hamiltonian of the system of interest, H_B the bath Hamiltonian, and H_{SB} their interaction. The system dynamical information is contained in the reduced density matrix $\rho(t)$, defined by taking the trace of the overall system $\rho_{tot}(t)$ over the bath degrees of freedom.

To show the purpose of the present work on the effect of a chirped excitation on extending the lifetime of vibronic coherences, we focus on a well-known photophysical process, *i.e.* the ultrafast intramolecular charge-transfer. In this work we focus on the P3HT:PCBM organic photovoltaic blend. Upon photo-excitation, an exciton delocalization is created along the polymer chain (the local excitation), and within a sub-100 fs timescale, a electron-transfer process takes place to a charge-transfer state, leaving a charge-separation between the P3HT (donor) and the

PCBM (acceptor). An illustration of the blend is shown in Fig. 2, with a close-up of the dimer adduct at the heterojunction.

H_S represents a P3HT:PCBM dimer adduct from the blend, such as the highlighted in the close-up on Fig. 1. A detailed description of how H_S has been modelled as first principles calculations is contained in Section 2.1.1. The bath Hamiltonian H_B describing the collective effect of the blend environment surrounding a specific dimer adduct, and the system–bath interaction H_{SB} Hamiltonian are further discussed in the following Section 2.1.2.

2.1.1 First-principles model of the system Hamiltonian. A linear vibronic coupling model[57] with a constant coupling was used to describe the dimer adduct Hamiltonian H_S. Here, the system Hamiltonian H_S is defined in the electronic space by a ground and a excited state Hamiltonians,

$$H_S = H_g + H_e, \quad (2)$$

where H_e represents an ensemble of two coupled electronic states. Making use of the diabatic representation of the electronic states ($|g\rangle$, $|e\rangle$) the two contributions can be written as

$$H_g = |g\rangle h_g \langle g|, \quad (3)$$

$$H_e = \sum_e |e\rangle(h_e + E_e)\langle e| + \sum_{e \neq e'} V_{ee'}|e\rangle\langle e'| \quad (4)$$

for e and e' running from 1 to 2. Here, h_g and h_e represent the vibrational Hamiltonians for the different electronic states, and E_e and $V_{ee'}$ are the diabatic electronic excitation energies (to the energy minima of the excited states) and the electronic coupling, respectively. The highest electronic excited state $e = 2$ represents the locally excited $|LE\rangle$ state, and the lowest-lying electronic excited state is the charge-transfer $|CT\rangle$ state. For a single system coordinate Q_{sys} (dimensionless), the vibrational Hamiltonian in the harmonic approximation for the ground and excited electronic states is given by

$$h_g = \frac{\Omega}{2}(P_{sys}^2 + Q_{sys}^2), \quad (5)$$

$$h_e = \frac{\Omega}{2}(P_{sys}^2 + Q_{sys}^2) - \Omega \Delta_e Q_{sys}, \quad (6)$$

where P_{sys} and Ω are the momentum and the vibrational frequency of the coordinate system, respectively. Δ_e is the displacement of the two excited states. The system Hamiltonian introduced above represents the minimal model to describe charge-transfer processes following the photoexcitation.

Here, the $|LE\rangle$ state is optically bright, whereas the lower-lying $|CT\rangle$ state is optically dark. Hence, the raising and lowering components of the transition dipole moment operator are defined as

$$X = \hat{\mathbf{e}}\hat{\mu}_{g,LE}|G\rangle\langle LE|, \; X^\dagger = \hat{\mathbf{e}}\hat{\mu}_{g,LE}|LE\rangle\langle G|. \quad (7)$$

In eqn (7), $\hat{\mathbf{e}}$ denotes the unit vector of the polarization of the pulse, and $\mu_{g,LE}$ the electronic transition dipole vector, $\mu_{g,LE} = |\boldsymbol{\mu}_{g,LE}|$, $\hat{\mu}_{g,LE} = \boldsymbol{\mu}_{g,LE}/\mu_{g,LE}$. In this study, we set for convenience $\hat{\mathbf{e}}\hat{\mu}_{g,XT} = 1$.

A parametrization of the P3HT:PCBM heterojunction followed TDDFT calculations using the computational software Q-Chem 6.2[16] on dimer structures obtained from a MD trajectory on the P3HT:PCBM blend from previous work by some of the present authors.[41] The MD simulation was simulated for a total duration of 100 ns at a reference temperature of 298.15 K. Additional details of the simulation and trajectory parameters are provided in the SI. To represent the realistic conditions of the blend, the following protocol was adopted: several P3HT:PCBM dimer adduct structures were sampled from different regions of the blend. To reflect the configurational heterogeneity within the MD blend, we focused on a single MD snapshot containing dimers with markedly different relative orientations and inter-molecular distances. The relative orientation between the two species and the intermolecular distance was different for the dimers sampled. Only dimers with intermolecular distance between 3–5 Å were considered. The model parameters obtained from the TDDFT calculations include adiabatic excitation energies for the locally-excited and charge-transfer states, frequencies of the system vibrational modes, dimensionless displacements Δ_e and value of the electronic coupling. Single-point TDDFT calculations were performed on the selected geometry of the
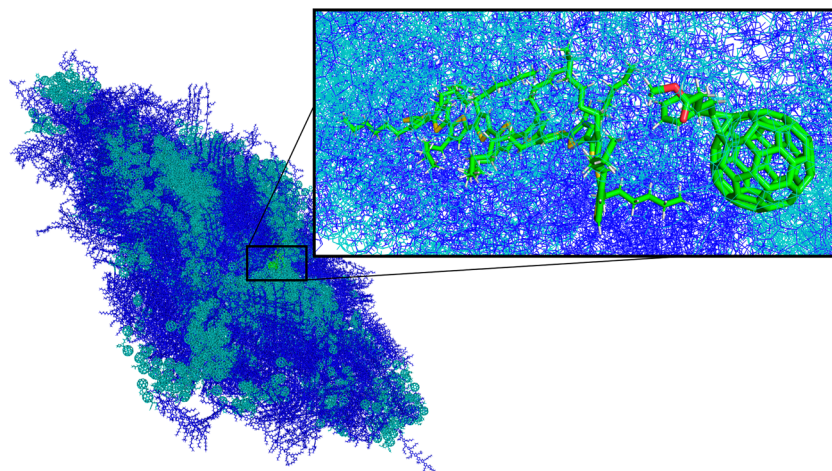

Fig. 1 Thin-film representation of the P3HT:PCBM blend with a close-up at the dimer heterojunction.

dimer adduct using the CAMB3LYP functional and 6-31+G* basis set, yielding the adiabatic excitation energies. The reason of performing the single-point excited state calculations on the geometries directly obtained from the blend, without performing a prior geometry optimization is the following: such an optimization would yield a geometry that deviates significantly from the true structure of the blend system. Which would lose the essential blend configurational information that we address in this study. It should be noted that the vibrational mode accounted for in the quantum dynamical simulations is a relatively high-frequency mode, corresponding to a stretching mode of the C=C bond in the P3HT backbone, therefore, its frequency is not expected to change significantly upon geometry optimization. The selection of the functional was made after carefully benchmarking several functionals including B3LYP and ωB97X-D. B3LYP, although widely used, is well known to underestimate excitation energies and fail to correctly describe CT states due to the lack of long-range correction. In our tests, ωB97X-D produced CT states with inconsistent orbital character (non-physical charge-transfer from the PCBM to the P3HT), complicating the reliable assignment of excitonic and CT transitions. In contrast, CAM-B3LYP yielded orbital characters and excitation energies in line with the expected physics of our system, offering a consistent and minimal long-range correction necessary for the accurate description of CT states. Following the orbital character and excited states analysis, described in the SI, CAM-B3LYP was chosen as the most appropriate functional for this system. To reduce the computational times, the hexyl groups of the P3HT have been substituted by methyl groups. This approach has been previously adopted in on theoretical studies on modelling the excitonic delocalization of P3HT[30,35,41] and it is shown that it does not affect the electronic and optical properties of the P3HT and similar conjugated polymers. Following a detailed analysis of the molecular orbitals for the first 20 electronic states in the dimer, the characterization of the excited states reveals the presence of a strong optically "bright" electronic state with locally-excited character on the P3HT (E_{LE} = 3.0402 eV). The lower-lying electronic states have a very low transition dipole, and can be viewed as optically "dark" states. Particularly, only one of them is associated with a charge-transfer character from the P3HT (donor) to the PCBM (acceptor), being the HOMO orbital in the P3HT and the LUMO orbital in the PCBM. Besides, these orbitals are also shared with the LE state, suggesting a strong charge-transfer coupling between both. The rest of electronic states below the locally excited state reveal a character of local-excitation on the PCBM unit. In a subsequent step, vibrational frequency and gradient and electronic coupling calculations associated to the LE and CT electronic states were performed on the selected dimer adduct. All the (mass weighted) normal modes of the system on the ground electronic state were calculated from TDDFT, and rescaled by $\sqrt{\Omega_i}$ to make them dimensionless. The excited-state potential energy surfaces are modeled as harmonic, with the same vibrational frequencies as the ground state. The displacements along the normal modes were reconstructed using excited-state gradient calculations at the MD snapshot geometry. To achieve this, the gradient obtained from TDDFT was transformed from Cartesian coordinates into dimensionless normal mode coordinates. The displacement for each mode was then determined by taking the ratio of the transformed gradient to the corresponding mode frequency. In this way, the gradient provides a direct estimate of the normal mode displacements upon excitation.[10] The diabatic electronic coupling was evaluated using the Boys diabatization method,[54] which has been previously demonstrated to be a good method for calculating intermolecular charge-transfer couplings. Further computational details of the TDDFT calculations can be found in the SI.

Out of the sample of dimers, two structures (dimers A and B) differing in intermolecular distance and relative orientation were selected to illustrate the message on this paper on the effect of chirped excitations. Table 1 summarises the system parameters in the diabatic representation for a one-dimensional model constructed on dimer A.

Table 1 highlights the vibrational frequency selected to model the vibronic dynamics of the system Hamiltonian H_S. This mode is the vibration with the largest displacement in the charge-transfer state and is the reaction mode that couples to the bath. The mode corresponds to a C=C stretch of the P3HT backbone.

Fig. 2 shows a sketch of the harmonic potential energy functions in the diabatic representation for the ground, first, and second electronic states. The validity of the displaced harmonic oscillator model for this type of systems has been previously validated in extensive theoretical studies by Burghardt et al.[57]

The model parameters of dimer B and additional dimers analysed from the blend are contained in the SI.

2.1.2 Hamiltonian of the dissipative environment. To model the dynamical effect of the environment on the intermolecular charge-transfer process, we consider the blend as a collection of infinite harmonic oscillators that are weakly coupled to the dimer system under study. Here the system–bath interaction is described using second-order linear response function, adopting the multilevel Redfield theory.[15,40,46] This serves as a reasonable approximation for capturing the dynamical fluctuations of the blend. As shown in previous work by Palacino-González et al.[41] on the same blend, first-principles TDDFT/MD simulations revealed that the thin-film morphology induces slow fluctuations in the system's electronic properties, resulting in long dephasing times extracted from the simulated 2D UV spectra. This observation supports the use of the Markovian approximation in our model, where the environment is assumed to evolve on a much slower timescale than the internal dynamics of the system. H_B and H_{SB} Hamiltonians from eqn (1) are described by

$$H_B = \sum_k \frac{\omega_k}{2}\left(p_k^2 + q_k^2\right), \tag{8}$$

Table 1 Model parameters in the diabatic representation derived from the TDDFT calculations on the dimer adduct

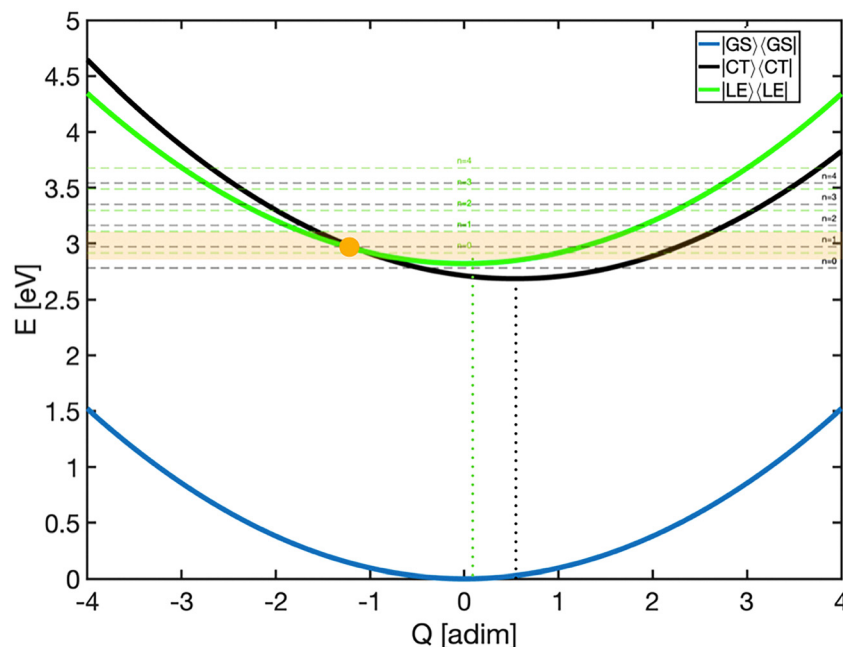| ε_{CT} [eV]	ε_{LE} [eV]	Δ_{CT} [adim.]	Δ_{LE} [adim.]	Ω [eV]	V [eV]
2.684	2.822	0.538	0.0037	0.190	−0.012

Fig. 2 Sketch of the parametrized diabatic potential energy functions for the dimer adduct investigated. Blue, black and green colours refer to the electronic ground, charge-transfer and locally-excited states, respectively. The lowest-lying vibrational states in the diabatic picture are shown. The crossing point between the two coupled excited states is indicated with a yellow circle. The energy region of the TL and chirped pulses used along this study is highlighted as a yellow shadowed area.

$$H_{SB} = Q_S \sum_k g_k q_k, \tag{9}$$

where p_k and q_k are the dimensionless coordinate and momentum operators from the bath, respectively, and g_k represents the system–bath coupling strength. The bath is characterized by the spectral density

$$J(\omega) = \frac{\pi}{2} \sum_k g_k{}^2 \delta(\omega - \omega_k). \tag{10}$$

which for the purpose of the present work it has been modelled phenomenologically.[15,40,61] Here we adopt an Ohmic function of the form

$$J(\omega) = \zeta \omega \exp\{-\omega/\omega_c\} \tag{11}$$

where ω_c is the bath "cut-off" frequency, which here equals the frequency of the system coordinate. Within the Redfield formalism, which offers a perturbative description of system–environment interaction, the dimensionless parameter ζ, characterizing the system–bath coupling strength, was set to 0.02 to ensure operation within the weak coupling regime.

2.2 Optical coupling to a linearly-chirped pulse

To investigate the influence of optical shaped pulses on the charge-transfer dynamics, a semi-classical description of system interacting with a oscillating laser field is adopted, with the total time-dependent Hamiltonian given by

$$H_{tot}(t) = H - H_F(t), \tag{12}$$

with $H_F(t)$ representing the interaction of the system with the external laser field.

In the dipole approximation and the rotating-wave approximation (RWA), the Hamiltonian describing the system–field interaction $H_F(t)$ is given by

$$H_F(t) = -\mu_{g,LE} \cdot E(t), \tag{13}$$

with $\mu_{g,LE}$ denoting the transition dipole from eqn (7) and $E(t)$ the temporal evolution of a general shaped pulse. For a Gaussian pulse, the latter can be written as

$$E(t) = \frac{1}{2} E_0 \exp\left(\frac{-t^2}{2T_0{}^2}\right) \exp(i\omega_0 t) e_z + \text{c.c.}, \tag{14}$$

with E_0, T_0 and ω_0 being the pulse amplitude, duration and carrier frequency.

In the present work we leverage the potential behind the properties of a linearly chirped pulse. The particularity of chirped pulses, which set them apart from their TL analogous is, that the carrier frequency evolves linearly in time. This results in a systematic temporal separation of frequency components, either increasing (negative chirp) or decreasing (positive chirp) across the pulse duration. As a consequence, the temporal evolution of the phase of a chirped pulse becomes quadratic, in contrast with the linear temporal evolution of a TL pulse phase. Despite this, chirping a TL pulse does not alter the energy information of the pulse, that is, the Fourier transform of the pulse temporal evolution does not change when chirping it. Here, we highlight that these properties within a chirped pulse can be seen as an additional tool to steer the dynamical evolution of a molecular system.

The temporal evolution of a linearly chirped Gaussian pulse is described by

$$E(\eta, t) = \frac{1}{2}E_{max}(\eta)F(\eta, t)\exp(i\phi(\eta, t))e_z + \text{c.c.} \quad (15)$$

with $\phi(\eta,t)$ representing the instantaneous phase given by

$$\phi(\eta, t) = \omega_0 t - \frac{\eta}{2T_0^2(1 + \eta^2)}t^2, \quad (16)$$

with η being the spectral chirp, also here referred to as the chirp parameter.

The temporal envelope of a chirped pulse, the maximum pulse amplitude and the effective pulse duration are described, respectively, by

$$F(\eta, t) = \exp\left(\frac{-t^2}{2T(\eta)^2}\right), \quad (17)$$

$$E_{max}(\eta) = \frac{E_0}{(1 + \eta^2)^{\frac{1}{4}}} \quad (18)$$

$$T(\eta) = T_0\sqrt{1 + \eta^2}. \quad (19)$$

Fig. 3 shows a sketch of a positively linearly chirped pulse (blue) and its TL analogous (black). Following the equations above, the sketch shows that when chirping a 15 fs TL pulse centred at $t = 0$ fs, the pulse amplitude becomes smaller at the centre of the pulse while its duration extends over a longer time (here ~ 400 fs). As previously discussed, both the TL and chirped pulse configurations contain the same total energy. The fundamental distinction lies in the temporal behaviour of their spectral components: in a TL pulse, all frequency components arrive simultaneously, whereas in a chirped pulse, the carrier frequencies, defined by the pulse's spectral resolution, arrive in a time-ordered sequence. This temporal evolution of the frequency within a chirped pulse is governed by the chirp parameter η.

For the simulations contained in Section 3, a base TL pulse of 15 fs pulse duration, carrier frequency $\omega_0 = 3.00$ eV and amplitude $E_0 = 0.001$ eV was used. Different chirped pulses were modelled for various values of $|\eta|$. The excitation energy region of the TL pulse and from its chirped versions is shadowed in yellow in Fig. 2.

2.3 Redfield quantum master equation

The dynamical evolution of the reduced density matrix $\rho(t)$ from Section 2.1.1 is described by quantum master equation

$$\frac{\partial}{\partial t}\rho(t) = -\frac{i}{\hbar}[H_S + H_F(t), \rho(t)] + (\mathcal{R} + \mathcal{D})\rho(t), \quad (20)$$

where $\mathcal{R}$ and $\mathcal{D}$ denote the Redfield and dephasing superoperators, respectively. The former accounts for both electronic and vibrational population relaxation, as well as electronic and vibrational dephasing, while the latter gives a phenomenological description solely of electronic dephasing.[15] Eqn (20) allows to treat explicitly the light-driven dynamics of the system in a nonperturbative manner. $\mathcal{R}$ denotes the Redfield relaxation (super) operator, which describes population relaxation and electronic dephasing due to the interaction with the dissipative bath. Its dependence on the external fields can be neglected in the weak-field coupling regime.

As introduced above, the Redfield superoperator is modelled here from Ohmic general spectral density functions. The dephasing superoperator $\mathcal{D}$, however, is modelled from previous work by some of the authors of the current paper, where a TDDFT/MD approach was developed to model electronic dephasing rates on the P3HT:PCBM blend.[41] This worked revealed typical electronic dephasing times of ~ 100 fs induced by the environment of P3HT and PCBM molecules in a thin-film structure.

The (super) operator $\mathcal{D}$ accounts for pure electronic dephasing and is given by

$$\mathcal{D}\rho(t) = -\zeta(|G\rangle\langle LE|\langle G|\rho(t)|LE\rangle + |G\rangle\langle CT|\langle G|\rho(t)|CT\rangle) + \text{H.c.} \quad (21)$$

where, ζ represents the phenomenological dephasing rate which, for simplicity, is taken the same for all electronic states.

Before the arrival of the laser pulse, the system is in thermal equilibrium in the electronic ground state

$$\rho(-\infty) = \rho_B|G\rangle\langle G|. \quad (22)$$

Here

$$\rho_B = Z_B^{-1}e^{-H_g/(k_BT)} \quad (23)$$

is a vibrational Boltzmann distribution (k_B is the Boltzmann constant, Z_B is the partition function, and T is the temperature).
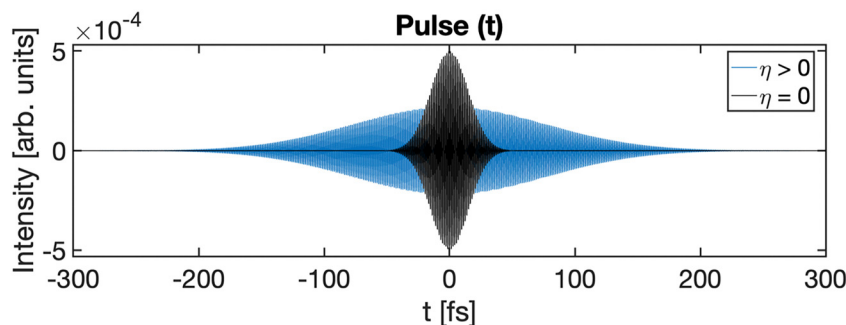

Fig. 3 Sketch of the TL pulse used (black) and its chirped analogous (blue) with $\eta = 5$.

To show the action of the Redfield operator R on the system dynamics explicitly, we write the eigenvalue solution of the system Hamiltonian H_S

$$H_S|\mu\rangle = E_\mu|\mu\rangle \tag{24}$$

from which the action of the Redfield operator R in eqn (20) is given by

$$[R\sigma(t)]_{\mu\nu} = \sum_{\kappa\lambda} R_{\mu\nu\kappa\lambda}\sigma_{\kappa\lambda}(t), \tag{25}$$

with $\sigma_{\kappa\lambda}(t) = \langle\kappa|\sigma(t)|\lambda\rangle$ denoting the matrix elements of the system density matrix in the eigenstate representation. $R_{\mu\nu\kappa\lambda}$ represents the Redfield tensor,[15,40] and is commonly written as

$$R_{\mu\nu\kappa\lambda} = \Gamma^+_{\lambda\nu\mu\kappa} + \Gamma^-_{\lambda\nu\mu\kappa}\delta_{\nu\lambda}\sum_\alpha \Gamma^+_{\mu\alpha\alpha\kappa} - \delta_{\mu\kappa}\sum_\alpha \Gamma^-_{\lambda\alpha\alpha\nu}. \tag{26}$$

The elements of the Redfield tensor can be written as

$$\Gamma^+_{\lambda\nu\mu\kappa} = \langle\lambda|Q|\nu\rangle\langle\mu|Q|\kappa\rangle\int_0^t d\tau F(\tau)e^{-i\omega_{\mu\kappa}\tau} \tag{27}$$

$$\Gamma^-_{\lambda\nu\mu\kappa} = \langle\lambda|Q|\nu\rangle\langle\mu|Q|\kappa\rangle\int_0^t d\tau(F(\tau))^*e^{-i\omega_{\lambda\nu}\tau} \tag{28}$$

where

$$F(\tau) = \frac{1}{\pi}\int_0^\infty d\omega J(\omega)[(2n(\omega) + 1)\cos(\omega\tau) - i\sin(\omega\tau)] \tag{29}$$

denotes the correlation function of the bath, introduced in Section 2.1.2 and $n(\omega) = (e^{\omega/kT} - 2)^{-1}$ is the Bose distribution function. The propagation of eqn (20) is performed *via* converting the master equation into matrix form by an expansion in terms of the numerically computed eigenstates of the system Hamiltonian H_S and solved *via* the fourth-order Runge–Kutta integrator with stepsize 0.25 fs.

3 Results and discussion

3.1 Electronic population dynamics and wave packet analysis

Quantum dynamical simulations were performed model constructed on the P3HT:PCBM adduct. The evolution of the population probability in the three electronic states over time was simulated as

$$P = \text{Tr}\{|e\rangle\langle e|\rho_e(t)\}, \tag{30}$$

where $\rho_e(t)$ is the temporal evolution of the population dynamics of an electronic state $|e\rangle$, following the master equation eqn (20).

Fig. 4 illustrates the population probabilities of the (a) optically bright $|LE\rangle$ state and (b) and (c) dark $|CT\rangle$ state following excitation with a single pulse. Panel (b) shows the data for different positive chirps scenarios, while the lower panel displays data for negative values of the chirp intensity η. Before the arrival of the pulse, the system is in a thermal equilibrium, following a Boltzmann distribution in the ground electronic state. Upon the pulse arrival, centred at $t = 0$, $|LE\rangle$ gets slowly populated. Panel (a) shows that for a chirp intensity

of $\eta = 5$, chirping the excitation (blue, red) results in a threefold increase in the population of $|LE\rangle$ at long times, once the pulse has gone, in contrast to the excitation with a TL case (black line). Besides, due to the effectively longer duration of a chirped pulse, the excitation of the ground electronic state happens earlier than for the TL, approximately by 150 fs. As a consequence of the longer pulse duration, the population of $|LE\rangle$ extends over a longer period, proportional to the pulse duration. Particularly, for the case of negative chirp, periodic beatings are observed to be more pronounced, reflecting a stronger coherent superposition of the different vibrational states excited. An interpretation for this is that chirping the excitation allows the pulse frequency to match the resonance condition with the vibrational energy levels of the system, promoting the creation of constructive interferences, which enhances population transfer to $|LE\rangle$. In contrast, a TL pulse lacks this time-dependent resonance, leading to less efficient excitation and a reduced population in $|LE\rangle$. As a consequence of the favoured excitation with a chirped pulse, the population of the dark charge-transfer state also increases when the excitation is chirped, as can depicted in panels (b) and (c), in contrast to the unchirped excitation case (black line). The simulations reveal two key phenomena. First, due to the effectively longer duration of a chirped pulse, with a phase evolving quadratically with time, the sign of the chirp can delay (positive chirp) or advance (negative chirp) the population of $|CT\rangle$. Our simulations show that increasing the intensity of the chirp parameter enhances this effect. This provides a potential method for indirectly controlling the population of an optically dark state over time. Second, the periodic oscillations of ~ 90 fs period observed in panels (b) and (c), reflects that the vibronic structure of the system are enhanced when chirping the excitation. An interesting effect observed is the phase-shift of the population dynamics when increasing the intensity of the chirp.

The effect of chirping the excitation can be seen by exploring the photoinduced wave packet under different pulse excitation conditions. The vibrational density of an electronic state, given by the electronic state density matrix in the space representation defined by the reaction coordinate in the system, Q, can give information about the wave packet. Fig. 5 depicts the time evolution of the wave packet in the dark electronic state, for different pulse excitation conditions. The simulations with a TL pulse excitation (a) reveal a delocalized wave packet along the coordinate space Q, that slowly relaxes due to the effect of the dissipative environment after an almost instantaneous creation with the pulse. The wavepacket is quasi-instantaneously created at $Q = 0$, revealing the transfer to the dark electronic $|CT\rangle$ state from the bright electronic $|LE\rangle$ state, is almost immediate after excitation. Panel (a) shows the motion of the wavepacket along the $|CT\rangle$ potential, displaying the vibronic beatings as a consequence of the electronic coupling between the two electronic states. The wave packet oscillates along the potential displaying a localized behaviour around $Q \sim 1.5$, and broadening along the rest of the coordinate space. A node is observed at $Q \sim 0.5$ in the wavepacket evolution before dissipation takes place at long times. This feature originates from the interference phenomena
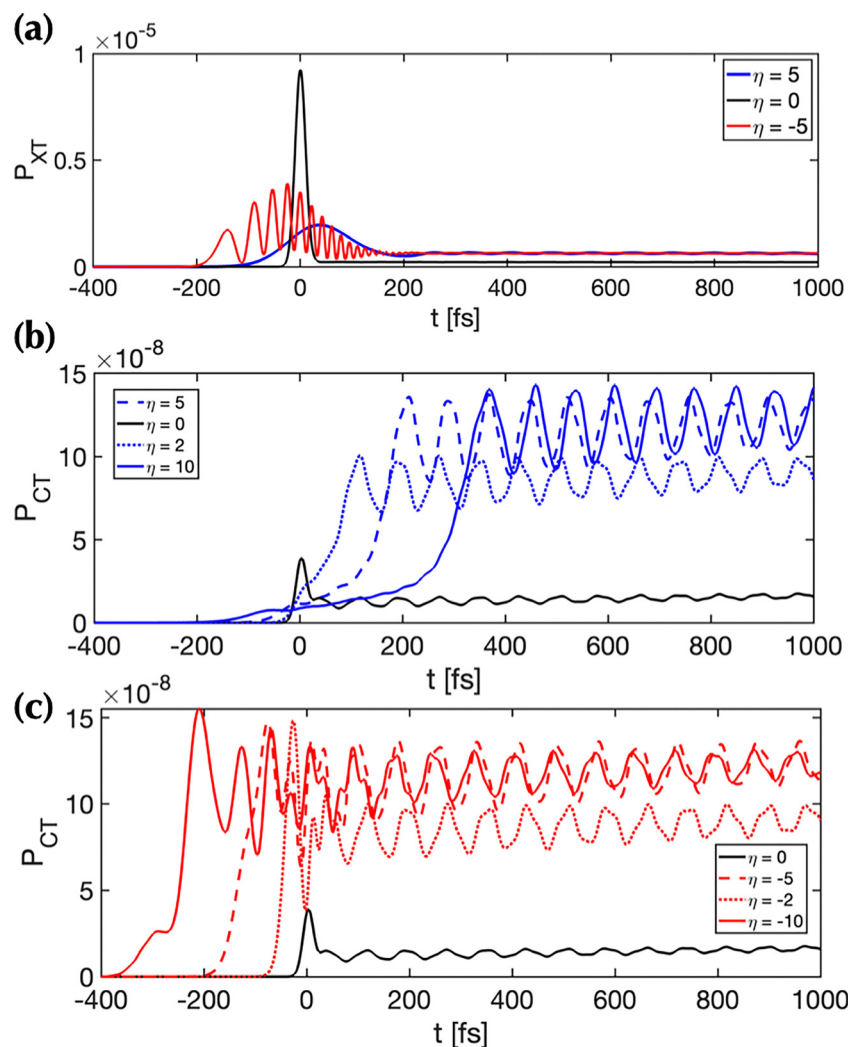
Fig. 4 Population probability of the (a) |LE⟩ and (b) and (c) |CT⟩ states over time for various pulse excitation conditions. Color legend: black – TL pulse, blue – positive chirp, red – negative chirp.

originated during the formation of the wave packet, and it is determined by the system–pulse interaction. Along time, the wave packet slowly dissipates to the minima of the |CT⟩ state at $Q = 0.5$. When the excitation is chirped, two key things happen to the wave packet, which manifest differently depending on the sign of the chirp parameter, η. First is a localization of the wave packet along the potential. Panels (c), (e), (g) and (d), (f), (h) show that the chirped excitation localizes the wave packet along the potential, in contrast to the unchirped excitation case displayed in (a). In particular, the beatings appears to be more localized in two return points at the dark-state potential, reflecting a more localized scenario, revealing enhanced vibrational quantum coherence signatures. This occurs independently on the sign of the chirp parameter, however, for the negative chirp case, vibrational features are even more enhanced with the chirp. Second, when increasing the value of the chirp, the final creation time of the wave packet is shifted along time, and increases with the intensity of the chirp. For a positive chirp (c), (e) and (g), the wave packet is delayed in time, whereas for the case of a negative

chirp (d), (f) and (h), a similar effect is observed, where the wave packet appears to be more localized along the potential and the vibrational quantum coherence features are enhanced. A significative difference with respect to the positive chirp scenario depicted is, that the creation of the wave packet is shifted to earlier times when increasing the value of the chirp. This time shift in wave packet creation (whether to earlier or later times) arises from the temporal evolution of the pulse's carrier frequency. In the case of a positive chirp, the higher vibrational levels of the bright state are initially excited, followed by the excitation of lower-lying vibrational states as the frequency decreases over time. Conversely, for a negative chirp, the excitation process occurs in the opposite order, with lower vibrational levels being excited first and higher levels excited later. These different excitation pathways leads to distinct interference patterns, resulting in a delayed wave packet formation for the positive chirp case and an earlier wave packet for the negative one. The nodal signature at $Q \sim 0.5$ is still observed when the pulse is chirped. An important aspect to consider is, that the
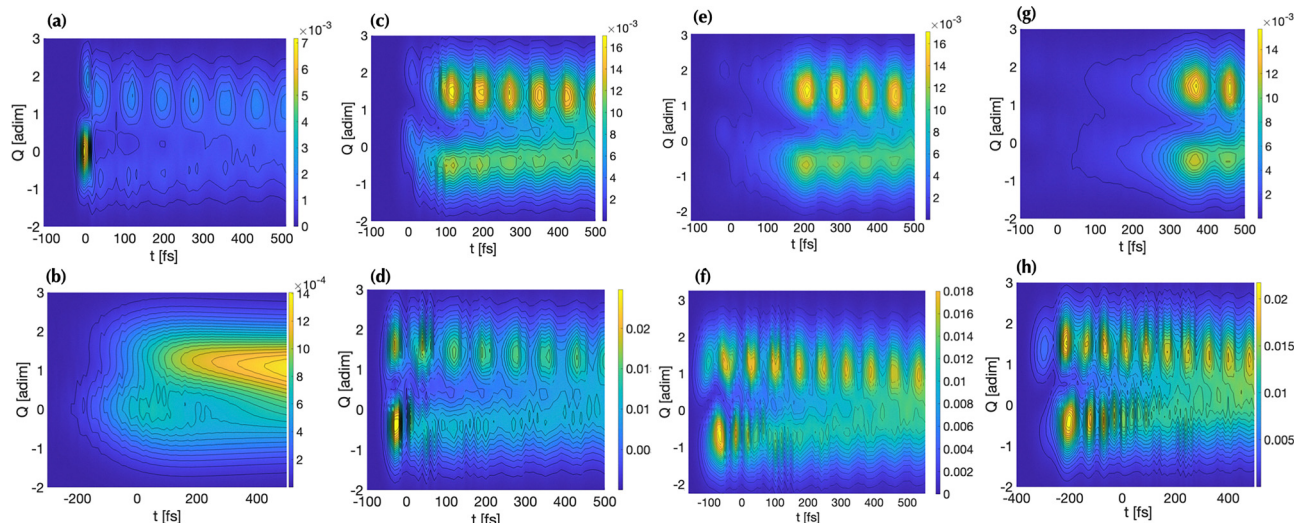
Fig. 5 Time evolution of wave packets in the $|CT\rangle$ state for different pulse excitation conditions. (a) TL pulse; 200 fs (b) long TL pulse; (c) positive chirp with $\eta = 2$, (e) $\eta = 5$, (g) $\eta = 10$; (c) negative chirp with $\eta = -2$, (e) $\eta = -5$, (g) $\eta = -10$.

observed effects are not a mere consequence of a longer inter-action with the pulse. To check the effect of the pulse interaction time one the shift experienced on the wave packet, an interaction with a TL pulse of similar effective duration to the one in panels (c) and (d), ~ 200 fs is simulated, shown in panel (b). We observe that even though the interaction with the pulse is present for a longer time, the creation time of the wave packet is not shifted from the central arrival time of the pulse ($t = 0$ fs). This indicates that the shift described on the creation time of the wave packet in the dark state potential is not due to the longer interaction time, but to the phase interference between the oscillatory phase of the chirp and the one associated to the originating wave packet.

3.2 Wigner functions and quantum coherences analysis

The effect of the chirp on the vibrational quantum coherences is further investigated by analysing the Wigner distribution functions (WDF) after excitation with a single TL pulse (a), and a positively (b) and negatively (c) chirped pulses. The WDF is a real object that describes the quasi-probability distribution function of a quantum state in the phase space representation, given by

$$W(Q, P) = \frac{1}{\pi\hbar}\int_{-\infty}^{\infty}\left\langle Q + \frac{s}{2}|\hat{\rho}|Q - \frac{s}{2}\right\rangle e^{-ips/\hbar}ds. \quad (31)$$

The analysis of the WDF provides information about the quantum phenomena in a system, such as the the presence of quantum coherence and interference effects. Fig. 6 shows the WDF for the vibrational density in the $|CT\rangle$ state. The vertical axis is the vibrational coordinate Q in the system and the horizontal axis represents the momentum P. Exciting the system with a pulse of constant carrier frequency leads to a wave packet that oscillates harmonically along the potential defined by Q. The negative region present in the WDF, that reflect the quantum coherence character of the wave packet, originates with the arrival of the pulse at ~ 20 fs. These

vibrational coherences survive up to ~ 500 fs, slowly dissipating due to the weak interaction with the bath. As previously describes in the population dynamics and wave packet analysis section, chirping the excitation introduces key differences in the photoinduced dynamics. This is reflected in the WDF as two main signatures. First, the maxima intensity of the WDF is shifted in time with respect to the central arrival time of the pulse, at $t = 0$ fs, depending on the direction of the chirp, in consonance with the wave packet simulations. Second, the quantum coherence signatures (blue features) survive for a longer time when the pulse is chirped (b) and (c). An interesting effect observed is the revival of the negative features in the positive chirped WDF for > 340 fs, for the pulse conditions used. This hints to a weak reversibility of the wave packet within the dissipative bath, which brings back the non-classical behaviour of a dissipating wave packet.

The appearance of negative values in the WDF is a crucial hallmark of quantum phenomena, being an indicator of non-classicality. This offers a powerful tool for quantifying quantum coherence and revealing non-classical effects such as super-position and entanglement. A convenient measure of this has been previously introduced as defined by the negative volume fraction,[19] given by

$$\delta_-(t) = \frac{\iint dp\,dq[|W(p,q;t)| - W(p,q;t)]}{\iint dp\,dq\,W(p,q;t)}, \quad (32)$$

and plotted in Fig. 7(a) and (b) for two different values of η. The information contained in the Wigner functions is confirmed by the data presented here. For $|\eta| = 5$, the duration of $\delta_-(t)$ ranges from approximately 500 fs in an unchirped excitation scheme to 650 fs with positive chirp and 800 fs with negative chirp. This indicates that introducing chirp extends the lifetime of vibrational quantum coherences by several hundred femtoseconds. To determine whether this effect is specific to a particular η value or remains consistent across different η values, δ_- is
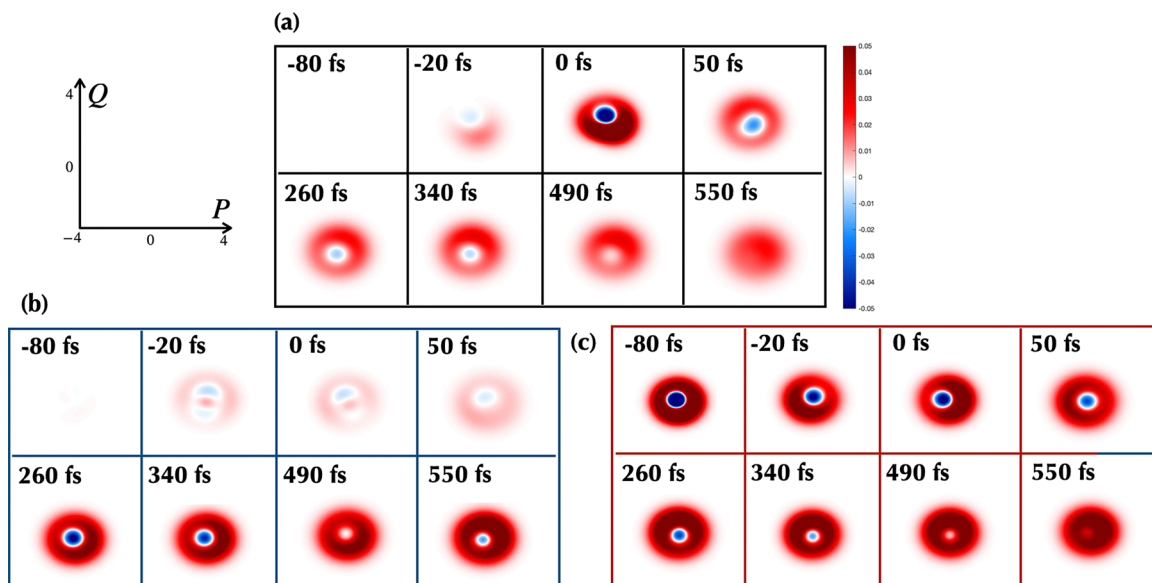
Fig. 6 Wigner distribution function (WDF) associated to the wave packet in the charge-transfer state over time for different chirp conditions. (a) TL pulse; (b) positively chirped pulse; (c) negatively chirped pulse. Vertical axis represents the coordinate space Q and horizontal axis represents the momentum space P. The scale of the axes is shown at the top left corner. The minimum of the $|CT\rangle$ potential is located at $Q = 0.5$.

measured for a larger chirp parameter, $\eta = 10$ (panel (b)). The results show that increasing the chirp further enhances the lifetime of quantum coherences even more significantly than for smaller chirp values. Starting from an initial coherence lifetime of 500 fs with a TL pulse, the use of a positively chirped pulse extends this lifetime to nearly 1 ps. For comparison, panel (b) also displays $\delta_-(t)$ for excitation with a long TL pulse, which generates only a minimal superposition of vibrational states in the system, resulting in an almost negligible $\delta_-(t)$.

3.3 Alternative model parameters and chirp effect

In this subsection, we present an alternative set of model parameters corresponding to dimer B to demonstrate that the

chirp effect extends beyond the previously studied system. These parameters were derived from first-principles calculations on a P3HT:PCBM dimer, employing the same TDDFT/MD formalism detailed in Section 2.1. The optimized geometry of the dimer adduct, the TDDFT-parametrized model data, and a schematic representation of the parametrized potentials are provided in the SI. This specific adduct was chosen because it exhibits two key differences from the previously analysed model. First, the crossing point between the two nonadiabatically coupled electronic excited states occurs at a higher mode displacement. Under identical excitation conditions, this positioning causes the photoinduced wave packet to originate from a lower-energy point on the bright-state potential relative to the crossing point.
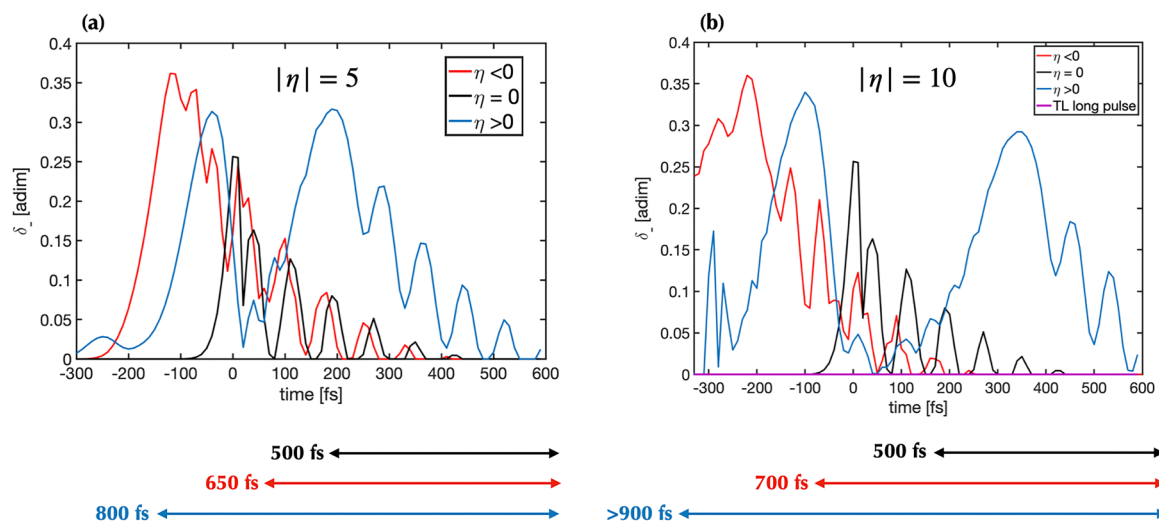

Fig. 7 Graph of the negative volume fraction associated to the WDF of the charge-transfer state for different chirp values of the excitation pulse. (a) $|\eta| = 5$, (b) $|\eta| = 10$. Below each panel, a representation of the lifetime of quantum coherences in the system is depicted.

This shift is expected to significantly influence the wave packet's transfer dynamics to the dark-state potential and, consequently, its lifetime. Second, the electronic coupling between the $|LE\rangle$ and $|CT\rangle$ states is substantially weaker in this model, with $V = 0.0002$ eV. Fig. 8 illustrates the data corresponding to this case. As observed in the original system, chirping the excitation shifts the population transfer to the charge-transfer state relative to the unchirped scenario. A positive chirp delays the initial transfer to the dark state, whereas a negative chirp advances it (see panel (a)). Additionally, increasing the chirp value enhances the vibrational features compared to the unchirped case. Analysis of the simulated wave packet in the charge-transfer state (panels (b)–(d)) under different chirp conditions supports our interpretation of this phenomenon. Similar to the original model, chirping extends the duration over which the wave packet is generated in the charge-transfer state. A positive chirp results in delayed wave packet formation, whereas a negative chirp advances it. A significant distinction between the two models emerges in terms of wave packet localization. While chirping consistently leads to a more localized wave packet, in this case, localization predominantly occurs on one side of the potential, around $Q \sim 1$. This behaviour can be understood by examining the potential energy surfaces of each model. When the crossing point is positioned at a higher displacement Q (see Fig. S5 in the SI), the coupled excited states maintain closer energy values over a broader range of Q, leading to a more delocalized wave packet on the dark electronic state. This contrasts with the previously analysed model, where the crossing point occurs at a smaller Q, resulting in a stronger wave packet localisation.

This theoretical observation offers a potential approach for estimating the position of a crossing between coupled states, which can be of experimental relevance. The comparison between the two models indicates that achieving wave packet localization *via* interaction with chirped pulses requires the excitation energy to be above the crossing point. This situation can be achieved by setting a detuning between the TL pulse central frequency and the system resonance energy, where the pulse energy is higher.

Last, the $\delta_-(t)$ was calculated for the WDF of the charge-transfer electronic state, along the propagation time, and it is shown in panel (e) of Fig. 8. The simulations reveal that the coherences lifetime extends from 40 fs to 500 fs and 900 fs when using a negative and positive chirped pulses, respectively. This suggests that the enhanced robustness of coherences due to chirping is an intrinsic property of a chirped pulse. The interference between the oscillatory phase of the chirp and that of the originating wave packet sustains these coherences for an extended duration, counteracting the effects of dissipation.

4 Conclusions

This study provides an in-depth analysis of how a chirped excitation influences electronic population dynamics, wave packet formation, and coherences lifetime in a electron donor–acceptor dimer system from the P3HT:PCBM blend. A first-principles-based model was parametrised from several
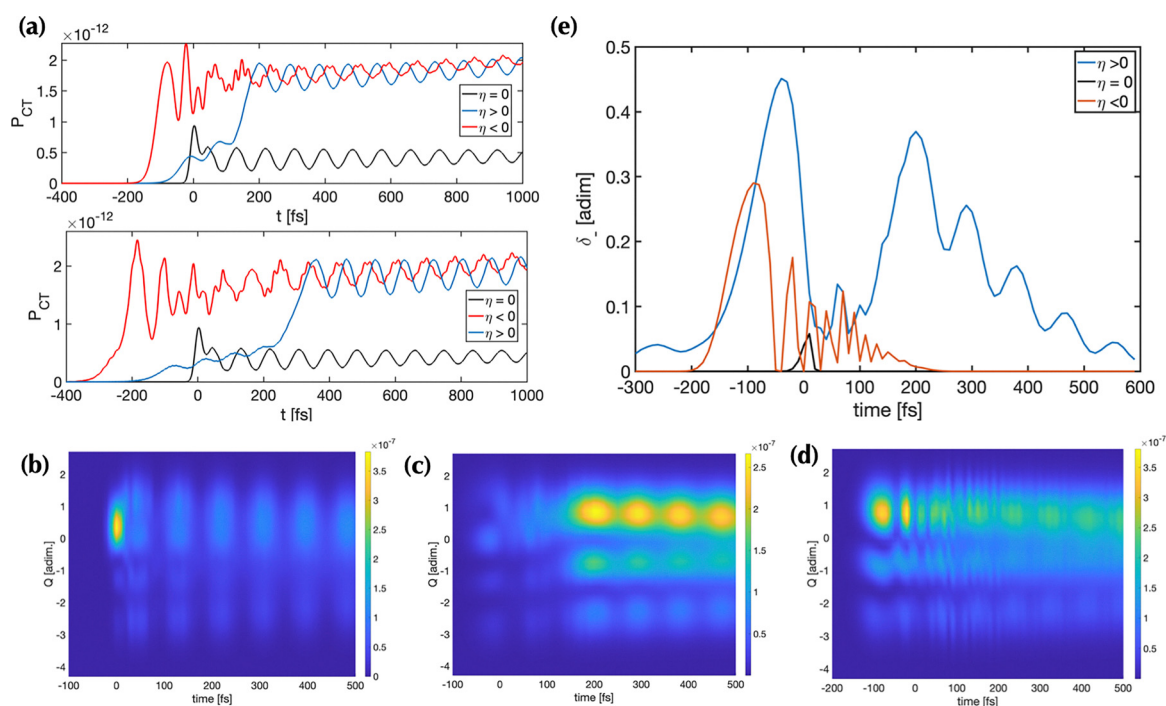

Fig. 8 Data for the additional dimer model analysed. Panel (a) shows the population probability of the charge-transfer state over time, for different pulse excitation conditions (upper panel: $|\eta| = 5$, lower panel: $|\eta| = 10$). Panels (b)–(d) show the wave packet evolution over time following a (b) TL, (c) positive chirp, and (d) negative chirp excitation. Panel (e) displays the negative volume fraction of the WDF in the charge-transfer state for the unchirped (black), positively (blue) and negatively (red) chirped excitation cases ($|\eta| = 5$).

dimer structures taken from the blend, and the effect of both positive and negative chirps in the excitation was explored. Using a linear vibronic coupling model and three electronic states (the ground state and two excited electronic states) with a dominant vibrational mode, we built two different models based on two different dimer structures in the MD blend.

The simulations show that chirping the excitation pulse significantly enhances the transfer of population to optically dark states and the vibronic features, in comparison to an excitation with a TL pulse. The analysis of the wave packets in the charge-transfer state for different chirp conditions shows that it is possible to exert some control on the formation time of the wave packet, advancing or delaying it over the TL excitation case. Besides, the chirp can serve as a tool to localise the wave packet in the charge-transfer state, affecting its overall lifetime before irreversible relaxation due to the interaction with the bath. The extent of the localization of the wave packet in the dark state is also sensitive to the relative displacements of the potentials. For crossing points located at small displacements at the excited states, the localization of the wave packet is strong, when using a chirped excitation. For higher crossings at higher energies, creating such localized wave packet requires a chirped excitation with a higher detuning of the pulse central frequency, being the resonance condition the energy difference between the minima of the ground state and the minima of the bright electronic state. A key observation, reported in this work, is the substantial impact of the chirp on the wave packet evolution, where the chirped pulse significantly extends the lifetime of vibrational coherences, supported by analysis of WDF for different excitonic conditions. This underscores the non-trivial interplay between the phase evolution of the excitation pulse and the intrinsic system dynamics. This insight is crucial for understanding how the temporal control in the excitation can determine the robustness of quantum systems over extended timescales.

The analysis presented in this work was extended to different sets of system parameters, derived from first-principles parametrisation of various dimer adducts within the blend. It was observed that these chirp-induced effects are generally present across adducts located in different regions of the P3HT:PCBM blend, indicating a broader behaviour characteristic of this type of donor–acceptor system. The two models used to illustrate this effect differed significantly in the displacements of the potential energy functions characterising the local excitation and charge transfer states, as well as in the strength of the electronic coupling. It was shown that the relative position of the crossing between the coupled electronic states plays a crucial role in determining the influence of the chirp on wave packet localisation and on extending the lifetime of light-induced vibronic coherences. In addition, it was demonstrated that by tuning the properties of the chirped pulse, such as the chirp intensity, the evolution of the field-induced dynamics can be substantially manipulated to achieve a desired target. These results provide evidence for a potential experimental route to indirectly estimate the position of crossings between coupled electronic states. At the same time, they

highlight the role of chirped pulses in enhancing the properties of light-induced systems, establishing the chirp as a promising tool to extend quantum coherence lifetimes. This holds relevance for the development of more efficient functional energy materials and for applications in the growing field of molecular quantum information science.

Overall, this work demonstrates the ability of chirped pulses to control both electronic and nuclear degrees of freedom in nonadiabatic systems modelled from first-principles, offering a promising strategy for the manipulation of quantum dynamics. Ongoing work is focused on extending these findings by modelling spectral bath densities from TDDFT/MD data, including a characterization of the dependence of the charge-transfer coupling along the fluctuating MD trajectory.

Conflicts of interest

There are no conflicts to declare.

Data availability

All the results contained in this work can be reproduced solely based on the data reported in the article. Additional data supporting this article has been included as part of the SI, including the optimized geometries for the adduct dimers selected from the blend, details of the TDDFT calculations and molecular orbital information. See DOI: **https://doi.org/10.1039/d5cp01684c**

For additional information, please contact the corresponding author.

References

1 R. Alessandri, J. J. Uusitalo and A. H. de Vries, *et al.*, Bulk heterojunction morphologies with atomistic resolution from coarse-grain solvent evaporation simulations, *J. Am. Chem. Soc.*, 2017, **139**(10), 3697–3705.

2 J. M. Anna, M. J. Nee, C. R. Baiz, R. McCanne and K. J. Kubarych, *J. Opt. Soc. Am. B*, 1993, **27**, 382–393.

3 C. J. Bardeen, Q. Wang and C. V. Shank, Selective excitation of vibrational wave packet motion using chirped pulses, *Phys. Rev. Lett.*, 1995, **75**(19), 3410.

4 B. Kaufman, P. Marquet, T. Rozgonyi and T. Weinacht, Long-lived electronic coherences in molecular wave packets probed by pulse-shape spectroscopy, *Phys. Rev. A: At., Mol., Opt. Phys.*, 2024, **110**, 033118.

5 C. Brif, R. Chakrabarti and H. Rabitz, Control of quantum phenomena: past, present and future, *New J. Phys.*, 2010, **12**, 075008.

6 D. Brinks, F. Stefani and F. Kulzer, *et al.*, Visualizing and controlling vibrational wave packets of single molecules, *Nature*, 2010, **465**, 905–908.

7 T. Brixner and G. Gerber, Quantum control of gas-phase and liquid-phase femtochemistry, *Chem. Phys. Lett.*, 2003, **4**, 418–438.

8 E. J. Brown, I. Pastirk, B. I. Grimberg, V. V. Lozovoy and M. Dantus, Population and coherence control by three-pulse four-wave mixing, *J. Chem. Phys.*, 1999, **111**, 3779–3782.

9 I. R. Sola, B. Y. Chang and B. Kim, *J. Chem. Phys.*, 2003, **118**, 6270–6279.

10 L. S. Cederbaum, H. Köppel and W. Domcke, Multimode vibronic coupling effects in molecules, *Int. J. Quantum Chem.*, 1981, **20**(S15), 251–267.

11 B. Y. Chang, S. Shin and I. R. Solá, *J. Chem. Phys.*, 2009, **131**, 204314.

12 D. Chen, A. Nakahara, D. Wei, D. Nordlund and T. P. Russell, P3HT/PCBM Bulk Heterojunction Organic Photovoltaics: Correlating Efficiency and Morphology, *Nano Lett.*, 2011, **11**(2), 561–567.

13 C. Cornaggia, J. Lavancier, D. Normand, J. Morellec, P. Agostini, J. P. Chambaret and A. Antonietti, *Phys. Rev. A: At., Mol., Opt. Phys.*, 1991, **44**, 4499–4505.

14 Q. Deng, J. Yu and H. Duan, *et al.*, The impact of pulse shaping on coherent dynamics near a conical intersection, *Photonics*, 2024, **11**, 511.

15 D. Egorova, M. Thoss and W. Domcke, *et al.*, *J. Chem. Phys.*, 2003, **119**, 2761.

16 E. Epifanovsky, *et al.*, Software for the frontiers of quantum chemistry: An overview of developments in the q-chem 5 package, *J. Chem. Phys.*, 2021, **155**(8), 084801.

17 S. M. Falke, C. A. Rozzi, D. Brida, M. Maiuri, M. Amato, E. Sommer, A. De Sio, A. Rubio, G. Cerullo and E. Molinari, *et al.*, Coherent Ultrafast Charge Transfer in an Organic Photovoltaic Blend, *Science*, 2014, **344**(6187), 1001–1005.

18 R. R. Frontiera, *J. Phys. Chem. B*, 2022, **126**, 5727–5729.

19 I. U. Goldschleger, M. N. van Staveren and V. A. Apkarian, Quantum tomography of a molecular bond in ice, *J. Chem. Phys.*, 2013, **139**, 034201.

20 G. Grancharov, M.-D. Atanasova, R. Kalinova, R. Gergova, G. Popkirov, C. Dikov and M. Sendova-Vassileva, Flexible Polymer-Organic Solar Cells Based on P3HT:PCBM Bulk Heterojunction Active Layer Constructed under Environmental Conditions, *Molecules*, 2021, **26**(22), 6890.

21 I. Gutiérrez-González, B. Molina-Brito, A. W. Götzc, F. L. Castillo-Alvarado and J. I. Rodríguez, Structural and Electronic Properties of the P3HT-PCBM Dimer: A Theoretical Study, *Chem. Phys. Lett.*, 2014, **612**, 234–239.

22 J. L. Herek, W. Wohlleben, R. J. Cogdell, D. Zeidler and M. Motzkus, *Nature*, 2002, **417**, 533–535.

23 M. Huix-Rotllant, H. Tamura and I. Burghardt, Concurrent Effects of Delocalization and Internal Conversion Tune Charge Separation at Regioregular Polythiophene-Fullerene Heterojunctions, *J. Phys. Chem. Lett.*, 2015, **6**, 1702–1708.

24 D. Jelovina, J. Feist, F. Martin and A. Palacios, *Phys. Rev. A*, 2017, **95**, 043424.

25 D. Keefer and R. de Vivie-Riedle, *Acc. Chem. Res.*, 2018, **51**, 2279–2286.

26 C.-H. Kim, S.-H. Cha, S. C. Kim, M. Song, J. Lee, W. S. Shin, S.-J. Moon, J. H. Bahng, N. A. Kotov and S.-H. Jin, Silver Nanowire Embedded in P3HT:PCBM for High-Efficiency Hybrid Photovoltaic Device Applications, *ACS Nano*, 2011, **5**(4), 3319–3325.

27 B. Kohler, V. V. Yakovlev and J. Che, *et al.*, Quantum control of wave packet evolution with tailored femtosecond pulses, *Phys. Rev. Lett.*, 1995, **74**, 3360.

28 F.-F. Kong, X.-J. Tian and Y. Zhang, *et al.*, Wavelike electronic energy transfer in donor-acceptor molecular systems through quantum coherence, *Nat. Nanotechnol.*, 2022, **17**, 729–736.

29 N. Liu, Y. Zhang, K. Niu, F. Lu and D. Zhong, Optical control of crossing the conical intersection in β-carotene, *J. Phys. Chem. Lett.*, 2023, **14**(41), 9215–9221.

30 T. Liu and A. Troisi, Absolute rate of charge separation and recombination in a molecular model of the p3ht/pcbm interface, *J. Phys. Chem. C*, 2011, **115**(5), 2406–2415.

31 S. A. Malinovskaya, T. Collins and V. Patel, *Advances in Quantum Chemistry: Ultrafast Manipulation of Raman Transitions and Prevention of Decoherence Using Chirped Pulses and Optical Frequency Combs*, Elsevier, ch. 7, 2012.

32 V. S. Malinovsky and J. L. Krause, *Phys. Rev. A: At., Mol., Opt. Phys.*, 2001, **63**, 043415.

33 V. S. Malinovsky and J. L. Krause, *Eur. Phys. J. D*, 2001, **14**, 147.

34 P. Marquetand, P. Nuernberger, T. Brixner and V. Engel, Molecular dump processes induced by chirped laser pulses, *J. Chem. Phys.*, 2008, **129**(7), 074303.

35 D. P. McMahon, D. L. Cheung and A. Troisi, Why holes and electrons separate so well in polymer/fullerene photovoltaic cells, *J. Phys. Chem. Lett.*, 2011, **2**, 2737–2741.

36 A. Ng, X. Liu, W. Y. Jim, A. B. Djurišic, K. C. Lo, S. Y. Li and W. K. Chan, P3HT:PCBM Solar Cells – the Choice of Source Material, *J. Appl. Polym. Sci.*, 2014, **131**(2), 39776.

37 R. Numico, A. Keller and O. Atabek, Laser-induced molecular alignment in dissociation dynamics, *Phys. Rev. A: At., Mol., Opt. Phys.*, 1995, **52**, 1298.

38 C. P. Oberg, L. C. Spangler, D. F. Coker and G. D. Scholes, Chirped laser pulse control of vibronic wavepackets and energy transfer in phycocyanin 645, *J. Phys. Chem. Lett.*, 2024, **15**(28), 7125–7132.

39 A. Olaya-Castro, A. Nazir and G. R. Fleming, Quantum-coherent energy transfer: implications for biology and new energy technologies, *Philos. Trans. R. Soc., A*, 2012, **370**, 3613–3617.

40 E. Palacino-González, M. F. Gelin and W. Domcke, Analysis of transient-absorption pump-probe signals of nonadiabatic dissipative systems: ''ideal'' and ''real'' spectra, *J. Chem. Phys.*, 2019, **150**, 204102.

41 E. Palacino-González and T. la Cour Jansen, Modeling the effect of disorder in the two-dimensional electronic spectroscopy of poly-3-hexyltiophene in an organic photovoltaic blend: A combined quantum/classical approach, *J. Phys. Chem. C*, 2023, **127**, 6793–6801.

42 E. D. Potter, J. L. Herek, S. Pedersen, Q. Liu and A. H. Zewail, *Nature*, 1992, **355**, 66–68.

43 A. Bernardi, R. Po, A. Calabrese, C. Carbonera, G. Corso and A. Pellegrino, From Lab to Fab: How Must the Polymer Solar Cell Materials Design Change? – an Industrial Perspective, *Energy Environ. Sci.*, 2014, **7**(3), 925–943.

44 H. Rabitz, *New J. Phys.*, 2009, **11**, 105030.

45 S. R. Rather, G. D. Scholes and L. X. Chen, From coherence to function: exploring the connection in chemical systems, *Acc. Chem. Res.*, 2024, **57**, 2620–2630.

46 A. G. Redfield, *Adv. Magn. Reson.*, 1965, **1**, 1.

47 G. D. Scholes, A molecular perspective on quantum information, *Proc. R. Soc. A*, 2023, **479**, 20230599.

48 G. D. Scholes, G. R. Fleming and A. Olaya-Castro, *et al.*, Lessons from nature about solar light harvesting, *Nat. Chem.*, 2011, **3**, 763–774.

49 J. D. Schultz, J. L. Yuly and E. A. Arsenault, *et al.*, Coherence in chemistry: Foundations and frontiers, *Chem. Rev.*, 2024, **124**, 11641–11766.

50 F. Schüppel, T. Schnappinger and L. Bäuml, *et al.*, Waveform control of molecular dynamics close to a conical intersection, *J. Chem. Phys.*, 2020, **153**, 224307.

51 M. Shapiro and P. Brumer. *Quantum Control of Molecular Processes*. Wiley-VCH, 2011.

52 A. De Sio, F. V. D. A. Camargo, K. Winte, E. Sommer, F. Branchi, G. Cerullo and C. Lienau, Ultrafast Relaxation Dynamics in a Polymer:Fullerene Blend for Organic Photovoltaics Probed by Two-Dimensional Electronic Spectroscopy, *Eur. Phys. J. B*, 2018, **91**(236), 1–10.

53 J. H. Soh, T. la Cour Jansen and E. Palacino-González, Controlling the nonadiabatic dynamics of the charge-transfer process with chirped pulses: Insights from a double-pump time-resolved fluorescence spectroscopy scheme, *J. Chem. Phys.*, 2024, **160**, 024110.

54 J. E. Subotnik, S. Yeganeh, R. J. Cave and M. A. Ratner, Constructing diabatic states from adiabatic states: Extending generalized mulliken-hush to multiple charge centers with boys localization, *J. Chem. Phys.*, 2008, **129**, 244101.

55 Z. Sun, C. Wang, W. Zhao, Y. Zheng and C. Yang, *Phys. Chem. Chem. Phys.*, 2018, **20**, 20957–20962.

56 M. Taherpour and Y. Abdi, Monte Carlo Simulation for Investigation of Morphology Dependent Charge Transport in Bulk-Heterojunction Organic Solar Cells, *J. Phys. Chem. C*, 2019, **123**(3), 1527–1538.

57 H. Tamura, R. Martinazzo and M. Ruckenbauer, *et al.*, Quantum dynamics of ultrafast charge transfer at an oligothiophene-fullerene heterojunction, *J. Chem. Phys.*, 2012, **137**, 22A540.

58 R. Tempelaar, L. J. A. Koster, R. W. A. Havenith, J. Knoester and T. L. C. Jansen, Charge recombination suppressed by destructive quantum interference in heterojunction materials, *J. Phys. Chem. Lett.*, 2016, **7**(1), 198–203.

59 W. S. Warren, H. Rabitz and M. Dahleh, *Science*, 1993, **259**, 1581–1589.

60 M. R. Wasielewski, M. D. E. Forbes and N. L. Frank, *et al.*, Exploiting chemistry and molecular systems for quantum information science, *Nat. Rev. Chem.*, 2020, **4**, 490–504.

61 U. Weiss. *Quantum Dissipative Systems*. World Scientific, Singapore, 1999.

62 W. Wohlleben, T. Buckup, J. L. Herek and M. Motzkus, *ChemPhysChem*, 2005, **6**, 850–857.

63 W. Wohlleben, T. Buckup, J. L. Herek and M. Motzkus, Coherent control for spectroscopy and manipulation of biological dynamics, *ChemPhysChem*, 2005, **6**, 850–857.

64 M. Wollenhaupt and T. Baumert, Ultrafast laser control of electron dynamics in atoms, molecules and solids, *Faraday Discuss.*, 2011, **153**, 9–26.

65 Z. Xu, Y. Zhou, L. Groß, A. De Sio, C. Yung Yam, C. Lienau, T. Frauenheim and G. Chen, Coherent Real-Space Charge Transport Across a Donor-Acceptor Interface Mediated by Vibronic Couplings, *Nano Lett.*, 2019, **19**(12), 8630–8637.

66 Y. Zhang, N. Liu, K. Niu, X. Wang, J. Yang, F. Lu, J. Chen and D. Zhong, Optical coherent quantum control of ultrafast protein electron transfer, *Sci. Adv.*, 2025, **11**(16), eado9919.

67 C. Zhuang, C. R. Paul and X. Liu, *et al.*, Coherent control of population transfer between vibrational states in an optical lattice via two-path quantum interference, *Phys. Rev. Lett.*, 2013, **111**, 233002.